

Bayesian analysis of a relativistic hadronic model constrained by recent astrophysical observations

Bruno A. de Moura S.,¹ [★] César H. Lenzi,¹ Odilon Lourenço,^{1,2} and Mariana Dutra^{1,2} [†]

¹ Departamento de Física, Instituto Tecnológico de Aeronáutica, DCTA, 12228-900, São José dos Campos, SP, Brazil

² Université de Lyon, Université Claude Bernard Lyon 1, CNRS/IN2P3, IP2I Lyon, UMR 5822, F-69622, Villeurbanne, France

11 September 2023

ABSTRACT

We use Bayesian analysis in order to constrain the equation of state for nuclear matter from astrophysical data related to the recent measurements from the NICER mission, LIGO/Virgo collaboration, and probability distributions of mass and radius from other 12 sources, including thermonuclear busters, and quiescent low-mass X-ray binaries. For this purpose, we base our study on a relativistic hadronic mean field model including an $\omega - \rho$ interaction. Our results indicate optimal ranges for some bulk parameters at the saturation density, namely, effective mass, incompressibility, and symmetry energy slope (L_0). For instance, we find $L_0 = 50.79^{+15.16}_{-9.24}$ MeV (Case 1) and $L_0 = 75.06^{+8.43}_{-4.43}$ MeV (Case 2) in a 68% confidence interval for the 2 cases analyzed (different input ranges for L_0 related to the PREX-II data). The respective parametrizations are in agreement with important nuclear matter constraints, as well as observational neutron star data, such as the dimensionless tidal deformability of the GW170817 event. From the mass-radius curves obtained from these best parametrizations, we also find the ranges of $11.97 \text{ km} \leq R_{1.4} \leq 12.73 \text{ km}$ (Case 1) and $12.34 \text{ km} \leq R_{1.4} \leq 13.06 \text{ km}$ (Case 2) for the radius of the $1.4M_\odot$ neutron star.

Key words: stars: neutron – dense matter – methods: data analysis – gravitational waves

1 INTRODUCTION

Neutron stars (NS) are some of the most fascinating and mysterious objects in the universe. These ultra-dense celestial bodies, formed by the collapse of massive stars, offer a unique opportunity to study the properties of nuclear matter under extreme conditions, since their core contains matter up to around ten times the saturation density ($\rho_0 \approx 2.5 \times 10^{14} \text{ g/cm}^3 \approx 0.16 \text{ fm}^{-3}$). This environment is a suitable framework in order to test the many types of hadronic relativistic and nonrelativistic models, along with its huge amount of related parametrizations. In that direction, it is possible to select, or at least distinguish, among different models/parametrizations able to reproduce known properties of this astrophysical compact objects (Oertel et al. 2017; Lattimer 2012; Menezes 2021). On the terrestrial side, on the other hand, studies on heavy ion collisions provide some constraints on the equation of state (EoS) for symmetric nuclear matter (SNM) at densities around ρ_0 (Danielewicz et al. 2002; Fuchs 2006). Other studies based on chiral effective field theory (Hebeler et al. 2013; Drischler et al. 2016; Krüger et al. 2013) also give some constraints on the EoS for pure neutron matter (PNM).

Recent measurements of NS properties such as masses, radii, and tidal deformability, have opened the door to a new era of investigation on the nature of these objects by establishing new constraints to be satisfied by different models. Such observations include the detection performed by the LIGO and Virgo Collaboration (LVC) of gravitational waves emitted during the so-called GW170817 event, in which

the merge of two NS was registered (Abbott et al. 2017, 2018, 2019a), and data provided by the NASA’s Neutron Star Interior Composition Explorer (NICER) mission concerning the X-ray detection coming from the proximity of the pulsars PSR J0030+0451 (Riley et al. 2019; Miller et al. 2019) and PSR J0740+6620 (Miller et al. 2021; Riley et al. 2021). By using the Tolman-Oppenheimer-Volkoff equations (TOV) (Tolman 1939; Oppenheimer & Volkoff 1939), it is possible to create a link between a specific EoS and a unique mass-radius diagram, a plot in which some of these observational data can be represented. Therefore, different EoSs can be tested against the updated astrophysical constraints. In this paper, we follow this procedure by means of a Bayesian analysis, namely, a powerful computational tool that can be used to combine observational/experimental data with theoretical models to test and constraint them as much as possible, in order to search for suitable EoSs capable of reproducing the aforementioned stellar matter requirements (Traversi et al. 2020; Salinas & Piekarewicz 2023; Zhu et al. 2022). In this sense, works doing EoS inference with Bayesian methods from the LIGO-Virgo collaboration has also been made (Abbott et al. 2019b, 2020)

We intend to find parametrizations of a relativistic mean-field (RMF) hadronic finite-range model based on theoretical grounds of the so-called quantum hadrodynamics (QHD). It considers protons and neutrons interacting with each other through Yukawa-type potentials (Yukawa 1935), in which the nucleon-nucleon interaction range is regulated by the masses of the exchanged mesons. Furthermore, the attractive and repulsive strengths of this interaction are controlled by the free parameters of the model. We use a version of the RMF model that takes into account cubic and quartic self-interactions in the field σ (attractive, meson σ), along with a crossed

[★] Contact e-mail: bmoura@ita.br

[†] Contact e-mail: marianad@ita.br

interaction between the fields ω^μ (repulsive, meson ω) and $\vec{\rho}_\mu$. The latter represents the isovector meson ρ responsible for the asymmetry of the system (different number of protons and neutrons). The procedure adopted here is to obtain, from the Bayesian inference, the suitable ranges for some nuclear matter bulk parameters and generate, from these quantities, the optimal parametrizations of this RMF model. As input for the method, we furnish Likelihood functions extracted from 16 different sources of masses and radii from thermonuclear busters Özel et al. (2016), from quiescent low-mass X-ray binaries Özel et al. (2016), from NICER, and LVC. We show that these “best” parametrizations determined from this approach are able to describe symmetric nuclear matter, pure neutron matter, and properties of the stellar matter system as well (radius of the $1.4M_\odot$ neutron star, and tidal deformability, for instance).

In comparison to the study performed in Traversi et al. (2020), our work presents the following novelties: (i) we use a Lagrangian density for the relativistic model with a $\omega - \rho$ interaction included. This new term gives us the freedom of choosing one more isovector bulk parameter to be used in the Bayesian analysis. In our case, in addition to the symmetry energy slope, we also take the symmetry energy at 2/3 of the saturation density; (ii) the range used for the former is based on the study coming from the analysis of the PREX-II results for the ^{208}Pb neutron skin thickness (Essick et al. 2021; Estee et al. 2021; Yue et al. 2022; Reed et al. 2021); (iii) we used as one of the sources of the Bayesian analysis the recent observational data provided by the NICER mission with regard to the pulsar PSR J0704+6620 (Riley et al. 2021).

The paper is organized as follows. In Section 2 we present the theoretical framework of the RMF model used as well as the main equations defining the neutron star matter properties. In Section 3 we furnish the details of the Bayesian method and the inputs used. Section 4 is dedicated to the results of our study, and, finally, summary and final remarks are shown in Section 5.

2 THEORETICAL FRAMEWORK

2.1 Relativistic mean-field model and bulk parameters

The RMF model used here is described by the following Lagrangian density (Dutra et al. 2014; Li et al. 2008)

$$\begin{aligned} \mathcal{L} = & \bar{\Psi}(i\gamma^\mu \partial_\mu - M_{\text{nuc}})\Psi - g_\sigma \sigma \bar{\Psi}\Psi - g_\omega \bar{\Psi}\gamma^\mu \omega_\mu \Psi \\ & - \frac{1}{2}g_\rho \bar{\Psi}\gamma^\mu \vec{\rho}_\mu \vec{\tau}\Psi + \frac{1}{2}(\partial^\mu \sigma \partial_\mu \sigma - m_\sigma \sigma^2) \\ & - \frac{A}{3}\sigma^3 - \frac{B}{4}\sigma^4 - \frac{1}{4}F^{\mu\nu}F_{\mu\nu} - \frac{1}{4}\vec{B}^{\mu\nu}\vec{B}_{\mu\nu} \\ & + \frac{1}{2}m_\rho^2 \vec{\rho}_\mu \vec{\rho}^\mu + \frac{1}{2}m_\omega^2 \omega_\mu \omega^\mu + \frac{1}{2}\alpha g_\omega^2 g_\rho^2 \omega_\mu \omega^\mu \vec{\rho}_\mu \vec{\rho}^\mu, \end{aligned} \quad (1)$$

where the nucleon field is represented by the Dirac spinor Ψ . The scalar, vector, and isovector fields σ , ω^μ , and $\vec{\rho}_\mu$ represent the mesons σ , ω , and ρ , respectively. The antisymmetric tensors are given by $F_{\mu\nu} = \partial_\nu \omega_\mu - \partial_\mu \omega_\nu$, and $\vec{B}_{\mu\nu} = \partial_\nu \vec{\rho}_\mu - \partial_\mu \vec{\rho}_\nu$. The nucleon mass is $M_{\text{nuc}} = 939$ MeV and the mesons masses are m_σ , m_ω , and m_ρ . By using the mean-field approximation along with the Euler-Lagrange equations, it is possible to construct the energy-momentum tensor $T^{\mu\nu}$. From this quantity, one obtains pressure, and energy density, in this case, given by

$$\begin{aligned} P = \frac{\langle T_{ii} \rangle}{3} = & -\frac{1}{2}m_\sigma^2 \sigma^2 - \frac{A}{3}\sigma^3 - \frac{B}{4}\sigma^4 + \frac{1}{2}m_\omega^2 \omega_0^2 + \frac{1}{2}m_\rho^2 \vec{\rho}_0^2 \\ & + \frac{1}{2}\alpha g_\omega^2 g_\rho^2 \omega_0^2 \vec{\rho}_0^2 + P_{kin}^n + P_{kin}^p, \end{aligned} \quad (2)$$

and

$$\begin{aligned} \varepsilon = \langle T_{00} \rangle = & \frac{1}{2}m_\sigma^2 \sigma^2 + \frac{A}{3}\sigma^3 + \frac{B}{4}\sigma^4 - \frac{1}{2}m_\omega^2 \omega_0^2 - \frac{1}{2}m_\rho^2 \vec{\rho}_0^2 \\ & + g_\omega \omega_0 \rho + \frac{g_\rho}{2} \vec{\rho}_0 \rho_3 - \frac{1}{2}\alpha g_\omega^2 g_\rho^2 \omega_0^2 \vec{\rho}_0^2 + \varepsilon_{kin}^n + \varepsilon_{kin}^p, \end{aligned} \quad (3)$$

respectively, with the kinetic parts written as

$$P_{kin}^{p,n} = \frac{\gamma}{6\pi^2} \int_0^{k_{F_{p,n}}} \frac{dk k^4}{(k^2 + M^{*2})^{1/2}} \quad (4)$$

and

$$\varepsilon_{kin}^{p,n} = \frac{\gamma}{2\pi^2} \int_0^{k_{F_{p,n}}} dk k^2 (k^2 + M^{*2})^{1/2}. \quad (5)$$

$k_{F_{p,n}}$ is the nucleon Fermi momentum, and γ is the degeneracy factor. This kind of hadronic model gives rise to a modification in the nucleon rest mass. In this case, the effective Dirac mass (Chen et al. 2007; Typel 2018) reads

$$M^* = M_{\text{nuc}} - g_\sigma \sigma. \quad (6)$$

For the sake of convenience, we also define, from this quantity, the ratio $m_0^* = M^*(\rho_0)/M_{\text{nuc}}$, where ρ_0 is the saturation density. All the remaining thermodynamical quantities can be obtained through Eqs. (2) and (3). For instance, the nuclear matter incompressibility is found by taking $K = 9(\partial P/\partial \rho)$, with the respective value at the saturation density being $K_0 \equiv K(\rho = \rho_0)$, and the binding energy of the system is obtained as $E_0 \equiv \varepsilon(\rho_0)/\rho_0 - M$. For the isovector part, the symmetry energy for instance is $\mathcal{S}(\rho) = \frac{1}{8} \frac{\partial^2(\varepsilon/\rho)}{\partial y^2} \Big|_{y=\frac{1}{2}}$, with y being the proton fraction of the system.

In general, these bulk parameters can be used in order to write the density dependence of the energy density for symmetric nuclear matter (Dutra et al. 2012; Vidaña et al. 2009), namely,

$$E_{SNM} = E_0 + \frac{1}{2}K_0 x^2 + O(x^3), \quad (7)$$

with $x = (\rho - \rho_0)/3\rho_0$. Similarly, the density dependence of the symmetry energy in SNM can be written as (Centelles et al. 2009)

$$\mathcal{S} = J + L_0 x + O(x^2), \quad (8)$$

where the quantities J and L_0 are given, respectively, by

$$J = \mathcal{S}(\rho_0) \quad \text{and} \quad L_0 = \rho_0 \left(\frac{\partial \mathcal{S}}{\partial \rho} \right)_{\rho=\rho_0}. \quad (9)$$

It is worth mentioning that many hadronic models exhibit a strong correlation between the symmetry energy at the saturation density (J) and its slope (L_0) (Gandolfi et al. 2012; Hebeler et al. 2013; Santos et al. 2015; Drischler et al. 2020; Li et al. 2021). In order to reproduce this feature, we decide to use as input in our calculations the value of the symmetry energy at $\rho_{\text{cross}} = 2\rho_0/3$, namely, $\mathcal{S}_{2/3} \equiv \mathcal{S}(\rho_{\text{cross}})$. It was mathematically shown in Santos et al. (2015) that if different parametrizations of a specific bulk parameter $\mathcal{A}(\rho)$ cross each other when plotted as a function of ρ , then the bulk parameter defined as the derivative of \mathcal{A} with respect to the density, namely, $\mathcal{B}(\rho)$, can present a linear dependence with \mathcal{A} at the saturation point, i.e., \mathcal{B} can correlates with \mathcal{A} as $\mathcal{B}(\rho_0) = a + b\mathcal{A}(\rho_0)$. By using the notation of Santos et al. (2015), we named the density at which the parametrizations of \mathcal{A} cross each other as the crossing density. Notice that since $L(\rho)$ is defined as a derivative of $\mathcal{S}(\rho)$, then the study performed in Santos et al. (2015) can be used to impose the correlation between L_0 and J . In this case, we decided to use the crossing density given by $\rho_{\text{cross}} = 2\rho_0/3$ as suggested by Khan & Margueron (2013). It is worth emphasizing that $\mathcal{S}_{2/3}$ and L_0 are

the only isovector quantities used as input in the Bayesian analysis, differently from the case of [Drischler et al. \(2020\)](#), that uses the correlated bulk parameters J and L_0 also quantifying the related uncertainties.

As a remark, we mention that, in principle, hyperons would be included in the model. However, the inclusion of such particles in the system softens the equations of state. As a consequence, the model does not produce very massive stars in comparison with the case in which nucleons are the only degrees of freedom (the hyperon puzzle). Moreover, hyperons interactions are not completely determined and some assumptions need to be taken, which makes inevitable the proliferation of more coupling constants to be fixed in the model. In this work, we prefer to avoid such issues by keeping, for the sake of simplicity, only nucleons and mesons on the hadronic side of the stellar matter system.

Here we use some particular ranges for the bulk parameters ρ_0 , m_0^* , E_0 , K_0 , $S_{2/3}$, L_0 , and from them, we determine the six coupling constants of the model, namely, g_σ , g_ω , g_ρ , A , B and α . These parametrizations are used as input for the Bayesian analysis. The “best” parametrizations obtained as the output of this procedure are shown to satisfy the observational constraints on the mass-radius diagrams, as well as the tidal deformability of the GW170817 event. We show these results and the aforementioned ranges in Sections 3 and 4.

2.2 Neutron star matter and tidal deformability

For the calculation of the mass-radius diagrams, it is needed to solve the Tolman-Oppenheimer-Volkoff (TOV) equations given by ([Tolman 1939](#); [Oppenheimer & Volkoff 1939](#)), with the total pressure and energy density are given by,

$$p = P + \frac{\mu_e^4}{12\pi^2} + \frac{1}{3\pi^2} \int_0^{\sqrt{\mu_\mu^2 - m_\mu^2}} dk k^4, \quad (10)$$

and

$$\epsilon = \varepsilon + \frac{\mu_e^4}{4\pi^2} + \frac{1}{\pi^2} \int_0^{\sqrt{\mu_\mu^2 - m_\mu^2}} dk k^2 (k^2 + m_\mu^2)^{1/2}, \quad (11)$$

respectively. For the leptonic part of the system, we include muons (μ), with $m_\mu = 105.7$ MeV and massless electrons (e). For each baryonic density, one needs to consider charge neutrality condition and chemical equilibrium $\mu_n - \mu_p = \mu_e$ and $\rho_p - \rho_e = \rho_\mu$, where $\mu_{p,n}$ are the protons/neutrons chemical potentials. For the neutron star crust, we use the Baym-Pethick-Sutherland EoS ([Baym et al. 1971](#)) for a density range of $6.29 \times 10^{-12} \leq \rho \leq 8.91 \times 10^{-3} \text{ fm}^{-3}$.

In binary neutron star systems, such as that in which the LVC has detected for the first time the GW produced by the coalescence of two NS ([Abbott et al. 2017, 2018](#)), the induced quadrupole momentum in one star, due to the static tidal field generated by the companion one, is related to the so-called tidal deformability parameter λ . The dimensionless version of such quantity reads

$$\Lambda = \frac{2}{3} \frac{k_2}{C^5}, \quad (12)$$

given in terms of $C = M/R$ (compactness parameter) and k_2 (second

tidal Love number). The latter is calculated through

$$\begin{aligned} k_2 &= \frac{8C^5}{5} (1 - 2C)^2 [2 + 2C(y_R - 1) - y_R] \\ &\times \left\{ 2C[6 - 3y_R + 3C(5y_R - 8)] \right. \\ &+ 4C^3[13 - 11y_R + C(3y_R - 2) + 2C^2(1 + y_R)] \\ &\left. + 3(1 - 2C)^2 [2 - y_R + 2C(y_R - 1)] \ln(1 - 2C) \right\}^{-1}, \quad (13) \end{aligned}$$

with $y_R \equiv y(R)$. The function $y(r)$ is found by solving the differential equation, coupled to the TOV ones, given by

$$r(dy/dr) + y^2 + yF(r) + r^2Q(r) = 0, \quad (14)$$

with

$$F(r) = \frac{1 - 4\pi r^2[\epsilon(r) - p(r)]}{1 - 2m(r)/r}, \quad (15)$$

$$\begin{aligned} Q(r) &= \frac{4\pi}{g(r)} \left[5\epsilon(r) + 9p(r) + \frac{\epsilon(r) + p(r)}{\partial p(r)/\partial \epsilon(r)} - \frac{6}{4\pi r^2} \right] \\ &- 4 \left[\frac{m(r) + 4\pi r^3 p(r)}{r^2(1 - 2m(r)/r)} \right]^2. \quad (16) \end{aligned}$$

More details regarding the derivation of these equations can be seen in [Hinderer et al. \(2010\)](#); [Postnikov et al. \(2010\)](#); [Damour & Nagar \(2010\)](#); [Binnington & Poisson \(2009\)](#); [Hinderer \(2008\)](#).

3 BAYESIAN METHOD

The method used to apply the mass-radius relation constraints to the equation of state of the RMF model discussed before is presented in this Section, namely, the Bayesian analysis. This analysis is a way to test and constrain the models. In this approach, the main idea is the construction of a posterior probability via Bayes' Theorem ([Sivia & Skilling 2006](#); [Gelman et al. 2014](#)), that reads

$$P(\theta|D, \mathcal{M}) = \frac{P(D|\theta, \mathcal{M})P(\theta, \mathcal{M})}{P(D, \mathcal{M})}. \quad (17)$$

It allows the calculation of the probability distribution of a set of parameters θ , given the data D for a given model \mathcal{M} . The distribution $P(\theta|D, \mathcal{M})$ is called probability distribution function (PDF). It is the result of the joining of previous information, given by the prior probability $P(\theta, \mathcal{M})$ that reflects the knowledge before the data is considered, with the Likelihood function $P(D|\theta, \mathcal{M})$ that is the statistical data from some probabilistic models. The probability of the observable data D , $P(D, \mathcal{M})$, is known as the evidence and it can be treated as a normalization factor since it does not depend on the parameters θ ([Steiner et al. 2010](#); [Traversi et al. 2020](#)).

As stated in Section 2.1, we determine our six coupling constants of the model from the six bulk parameters m_0^* , E_0 , K_0 , ρ_0 , $S_{2/3}$, and L_0 . Based on different theoretical studies ([Souza et al. 2020](#); [Margueron et al. 2018](#); [Cai & Li 2016](#)), we decide to fix ρ_0 and E_0 because it is well established in the literature that their values are around 0.15 fm^{-3} and E_0 at -16.0 MeV, respectively, with very small error bars, as one can see for instance in [Margueron et al. \(2018\)](#), in which the ranges for such quantities are given by $\rho_0 = (0.155 \pm 0.005) \text{ fm}^{-3}$ and $E_0 = (-15.8 \pm 0.3) \text{ MeV}$. The remaining bulk parameters constitute our set θ and will be inferred by the Bayes' Theorem, Eq. (17). Different studies were performed in order to determine ranges for these bulk parameters, and we follow some of them to give input for the Bayesian analysis. For m_0^* , we chose the range found in [Souza et al. \(2020\)](#), namely, $0.60 \leq m_0^* \leq 0.88$. The range used for the incompressibility is $220 \text{ MeV} \leq K_0 \leq 260 \text{ MeV}$ ([Garg & Colò 2018](#)). In

Table 1. Ranges used in the priors. For saturation density and binding energy, we fix $\rho_0 = 0.15 \text{ fm}^{-3}$ and $E_0 = -16 \text{ MeV}$, respectively.

Prior	Range	m_0^*	K_0 (MeV)	$S_{2/3}$ (MeV)	L_0 (MeV)	
					Case 1	Case 2
Uniform	Min	0.60	220.0	22.45	38.0	69.0
	Max	0.88	260.0	26.04	143.0	107.8
Gaussian	Δ	0.74	240.0	24.25	90.5	88.4
	σ	0.07	10.0	0.90	26.25	9.7

the case of $S_{2/3}$, we take the range $22.45 \text{ MeV} \leq S_{2/3} \leq 26.04 \text{ MeV}$, obtained for the nonlinear RMF models found in Dutra et al. (2016) (excluding the density-dependent ones), see Table I of this reference. For the symmetry energy slope, we use the findings of recent studies that calculate L_0 based on the results for the neutron-skin thickness of ^{208}Pb experiment (PREX-II), $L_0 = 53^{+14}_{-15} \text{ MeV}$ (Essick et al. 2021), $L_0 = (106 \pm 37) \text{ MeV}$ (Reed et al. 2021), $42 < L_0 < 117 \text{ MeV}$ (Estee et al. 2021), $L_0 = (83.1 \pm 24.7) \text{ MeV}$ (Yue et al. 2022). As we also intend to investigate how different ranges of L_0 affect the PDF, we decide to split our priors into two cases, namely,

- **Case 1:** range determined by the lowest and the highest values of L_0 :

$$38 \text{ MeV} \leq L_0 \leq 143 \text{ MeV} \quad (18)$$

- **Case 2:** range determined by the the intersection of the L_0 values from Reed et al. (2021); Estee et al. (2021); Yue et al. (2022):

$$69 \text{ MeV} \leq L_0 \leq 107.8 \text{ MeV}. \quad (19)$$

In principle, different priors may alter the posteriors (Steiner et al. 2016). In order to verify this hypothesis, we calculate the latter by using Uniform and Gaussian prior distributions. In the case of the Uniform distribution, the global ranges for the bulk parameters presented before are used (minima and maxima values). With regard to the Gaussian distribution, we assign the respective mean value, $\Delta = (Max + Min)/2$, and deviation, $\sigma = (Max - Min)/4$, for each quantity. All the numbers used as input for the different priors are presented in Table 1.

It is important to emphasize here that in order to calculate the posteriors, we adopted a method widely used in the literature and detailed, for instance, in Steiner et al. (2010); Özel et al. (2016); Raithel et al. (2017); Traversi et al. (2020). In this case, the likelihood is the probability of generating N mass-radius observations given a particular set of empirical parameters. In our case, given an EoS, we calculate the probability of realization of the pair $D = (M, R)$ of a specific source through the following procedure: (i) given a set of empirical bulk parameters, we calculate the respective EoS and, from that, the corresponding mass-radius diagram. If the EoS produces $M_{\max} < 2M_{\odot}$, the particular parameters set is disregarded and another one is taken. (ii) If the condition $M_{\max} \geq 2M_{\odot}$ is satisfied, the probability of each star configuration of the mass-radius diagram is evaluated by using the $M - R$ distribution of the source. Then, we have

$$P(D|m_0^*, K_0, S_{2/3}, L_0, \mathcal{M}) = \prod_{i=1}^{n=16} P_i(D_i|m_0^*, K_0, S_{2/3}, L_0, \mathcal{M}), \quad (20)$$

where

$$P_i(D_i|m_0^*, K_0, S_{2/3}, L_0, \mathcal{M}) = P_{\max,i}(D_i|m_0^*, K_0, S_{2/3}, L_0, \mathcal{M}), \quad (21)$$

where $P_{\max,i}(D_i|m_0^*, K_0, S_{2/3}, L_0, \mathcal{M})$ is maximum probability associated with the parameter set.

The observational data are constituted of 16 sources, which are posterior probability distributions from masses and radii. 11 of them were extracted from Özel et al. (2016), where 6 are thermonuclear busters called 4U 1820–30, SAX J1748.9–2021, EXO 1745–248, KS 1731–260, 4U 1724–207, and 4U 1608 –52. The data of these sources are calculated by using their apparent angular diameters, distance, and touchdown fluxes. The 5 other sources, out of the 11 ones, were obtained from the following Quiescent Low-Mass X-ray Binaries (qLMXBs): M13, M30, NGC 6304, NGC 6397, and ω Cen, whose mass-radius posteriors are calculated from the spectroscopic analysis of the thermal radiation emission. All the explanation about these 11 sources, as well as the $M - R$ data distributions, can be found in Özel & Paulo (2016).

Regarding the 5 sources remaining, out of the 16 ones, one of them comes from the neutron star X-ray analysis in 4U 1702–429, see Nättilä, J. et al. (2017), in which the authors calculated $M = 1.9 \pm 0.3 M_{\odot}$ and $R = 12.4 \pm 0.4 \text{ km}$. From the LVC (Abbott et al. 2018) we use the 2 components coming from the analysis of the gravitational wave event GW170817, namely, the posterior mass-radius insensitive to EoSs (LSC et al. 2019). The last 2 sources come from mass-radius measurements obtained from the data provided by the NICER mission, namely, one for pulsar PSR J0030+0451, calculated through models for the pulsation profile (Riley et al. 2019), and another for pulsar PSR J0740+6620, calculated by using X-ray observations and rotating hot region patterns (Riley et al. 2021). In order to mimic the $M - R$ distributions for the 4U 1702–429 and PSR J0030+0451 observables, we use the same description and parameters proposed in Nättilä, J. et al. (2017); Traversi et al. (2020), namely, the bivariate Gaussian distribution.

Finally, the numerator of the PDF in Eq. (17) is calculated through the Markov Chain Monte Carlo (MCMC). For this purpose, we use the *emcee* python package presented in Foreman-Mackey et al. (2013). However, as our study considers 2 different priors, as well as 2 different sets of parameters L_0 , it is necessary to calculate the evidence $P(D, \mathcal{M})$. Such a quantity was obtained through a Monte Carlo integration over the posterior.

4 RESULTS

4.1 Bayesian analysis

Following the procedure detailed in the previous Section, we calculate the PDF by considering the description for the EoS shown in Section 2.1. As a first result, we display in Fig. 1 the posterior PDFs for the empirical parameters using Uniform prior distributions related to Case 1 and Case 2. For both cases, the effective mass shows a preference for larger values, presenting a very pronounced peak around the mean value. Notice that the histogram has a steep drop around $m_0^* = 0.8$. One of the reasons could be the upper limit of the interval chosen for the analysis (0.88), which is close to the most probable value. Both K_0 and $S_{2/3}$ present a flat behavior in its posterior. The incompressibility has a decreasing behavior and a trend of choosing lower values compared with the prior in both cases. Notice that for $S_{2/3}$, the final statistical analysis presents no abrupt changes in comparison with the uniform prior adopted for both cases. In particular, in Case 2 there is a general trend of increasing in the posterior in the direction of attaining the upper limit of the prior, namely, $\approx 26 \text{ MeV}$. This is the number pointed out in Reed et al. (2021) as being the correct value for $S_{2/3}$. The authors claim

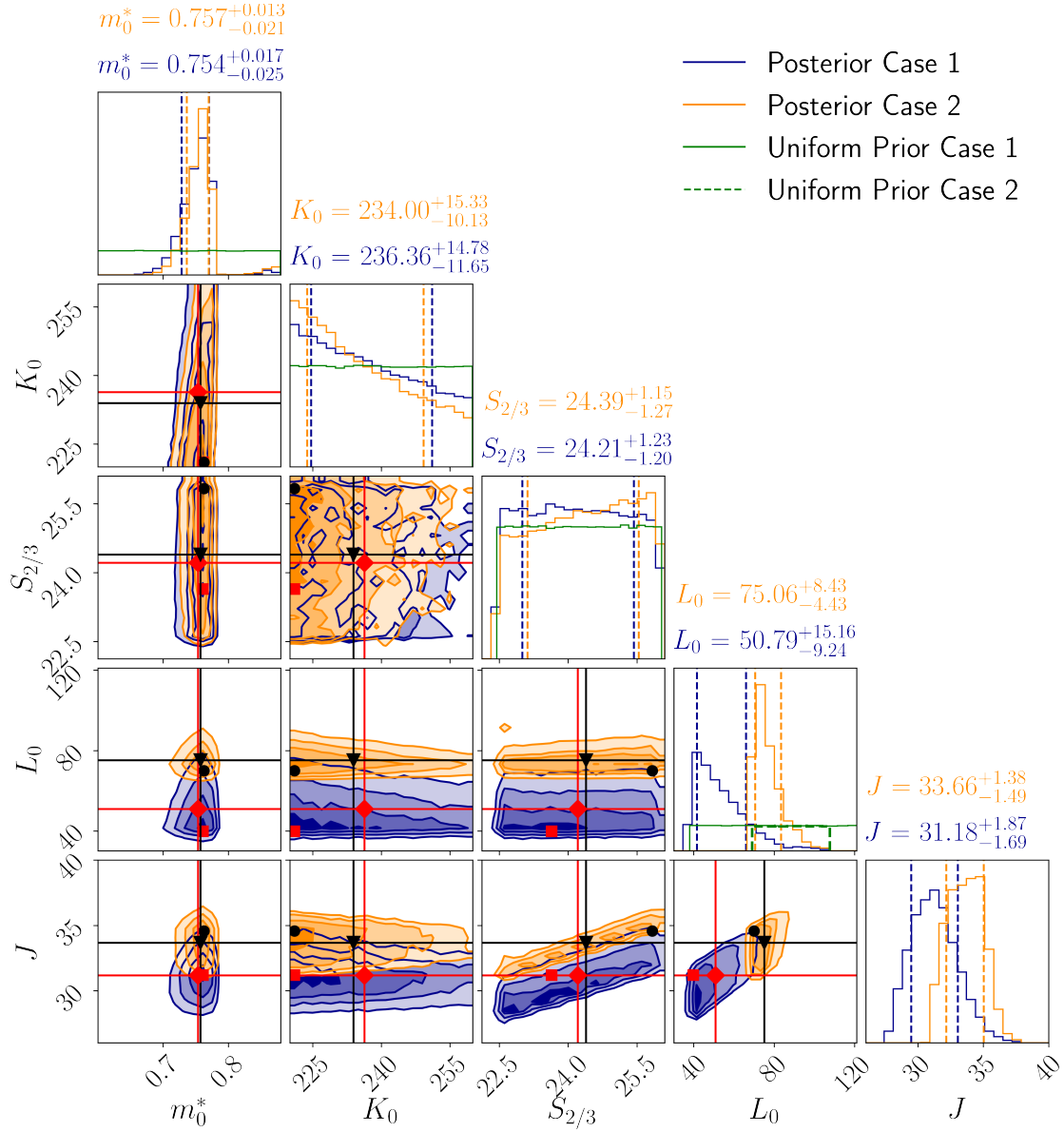


Figure 1. Posterior distribution of the bulk parameters using Uniform prior for Case 1 (orange) and Case 2 (blue). The histograms shown on the diagonal represent the posterior marginal distribution of each parameter independently. The solid black (red) lines represent the median value of PDF for Case 1 (Case 2). The blue (orange) dashed lines indicate the values for 0.16 and 0.84 quantiles for Case 1 (Case 2). The black (red) dot (square) points refer to the median values or the Case 1 (Case 2). The black (red) triangle (diamond) is the most probable value or the Case 1 (Case 2), i.e., the modes. The σ levels in the 2D histograms are 0.5σ , 1σ , 1.5σ , and 2σ . The prior limit is shown as a green line (dashed line) for Case 1 (Case 2) in the diagonal.

that $S_{2/3} \approx 26$ MeV since this quantity is tightly constrained by the binding energy of heavy nuclei. Concerning L_0 , we can observe a preference for smaller values for both cases. Nonetheless, due to the upper limit being greater in the range of Case 2, it allows the slope of the symmetry energy to obtain values greater than those obtained in Case 1.

After the calculation via Bayesian analysis, a 1D and 2D histograms were built for the values obtained for the symmetry energy in the saturation density, using the set of parameters obtained in the posterior distribution (see the last line of Fig. 1). Note that J is distributed centered for both cases. This distribution is highly likely to be less than ≈ 34 (≈ 36) MeV for Case 1 (Case 2) with a confidence interval (CI) of 90%. Although both distributions are centered, the

one for Case 1 produces the most probable values around 31 MeV against 34 MeV for Case 2.

By analyzing the posterior calculated using the Gaussian prior, Fig 2 one sees the same behavior for the effective mass as when the Uniform prior was used, that is, a sharp pick followed by a cut-off around 0.8 for both cases studied. The posterior distributions for K_0 and $S_{2/3}$ do not differ from the prior. For these three quantities, Cases 1 e 2 have practically a similar comportment. The same does not occur for L_0 , but the tendency to choose lower limit values is still the same. Both Cases have the posterior values shifted to the left in relation to their respective priors. For this quantity, the entire analysis with 90% CI allows intervals around 33 – 84 (64 – 93) MeV. The

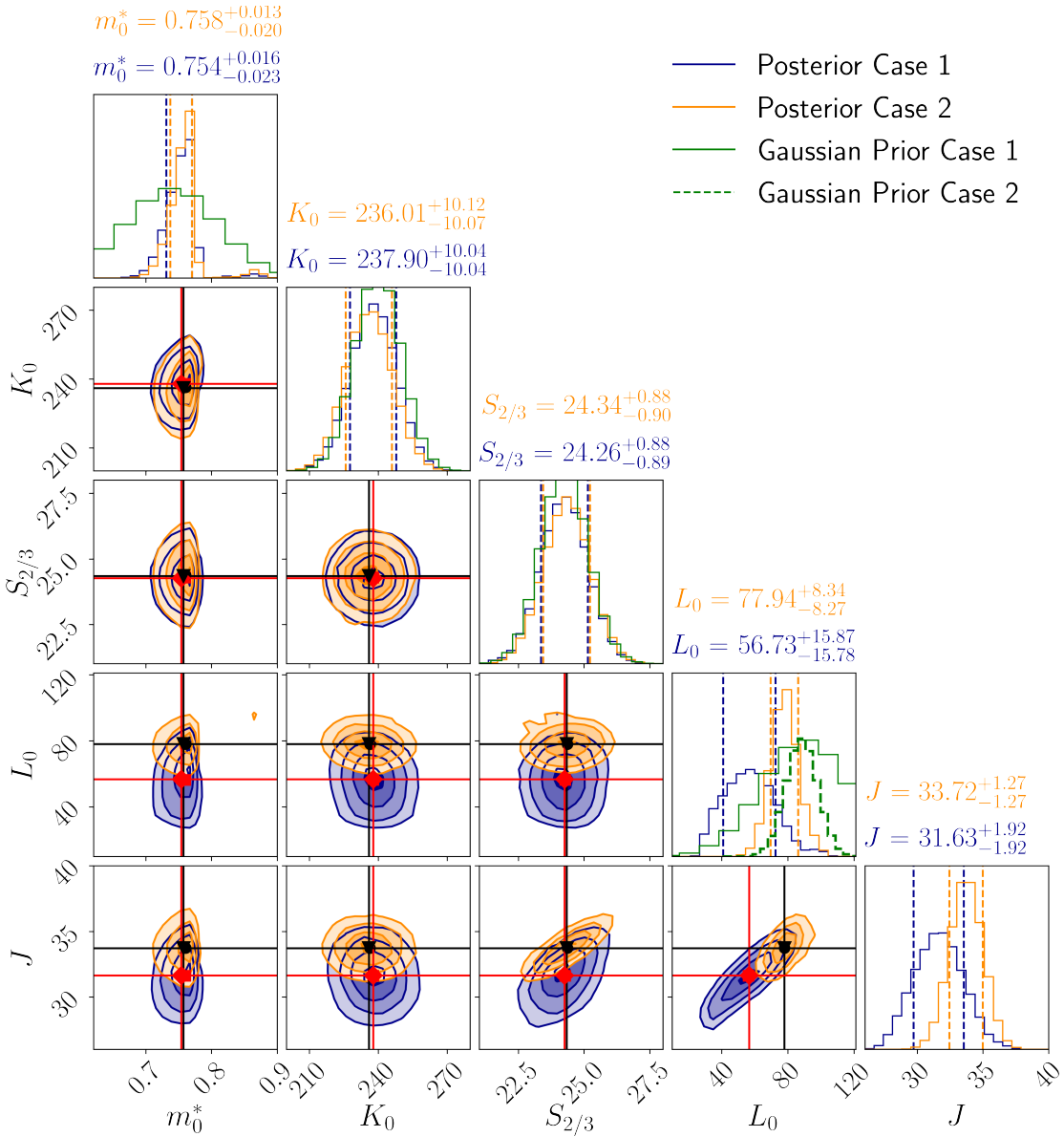


Figure 2. Posterior distribution of the bulk parameters using a Gaussian prior. The same notation as in Fig. 1.

most probable value for the symmetry energy found after the analysis is practically the same obtained in Fig 1, for Case 1 (Case 2).

The boundaries for the bulk parameters along with other statistical quantities such as mean, mode, and median are shown in Table 2 for the different priors used.

To test the hypotheses raised by the used models, that is, for the priors and cases chosen, it is interesting to calculate the Bayes factor (BF) (Jeffreys 1961; Robert et al. 2009; Köhlinger et al. 2019; Breschi et al. 2021). The Bayes factor can be found by reason of the evidence of two models:

$$\mathcal{B}_{AB} = \frac{P(D|\mathcal{M}_A)}{P(D|\mathcal{M}_B)} = \frac{Z_A}{Z_B}. \quad (22)$$

For the comparison, we define Case 1 as the set of parameters for \mathcal{M}_A . This assumption is made due to its less restrictive choice for the L_0 parameters. To interpret the BF we have used the suggestion proposed by Jeffreys (1961) and summarized in Kass & Raftery

(1995) given in Table 3. The results for the models used are shown in Table 4 and Table 5.

We can see a slight preference for the description that uses the uniform prior with the set of parameters defined in Case 2. This shows the preference for lower values of L_0 , in agreement with recent studies that point out smaller ranges for this quantity. For example, we can quote the range of $L_0 = (54 \pm 8)$ MeV Reinhard et al. (2021). In this study, the authors determine the value of L_0 by analyzing the parity violation in ^{208}Pb . Still using the lead core, the reference Hu et al. (2022) found the range of $L_0 = (37 - 66)$ MeV using ab initio calculations. Recently, an analysis via Bayesian inference, taking into account the results of PREX-2 and CREX Zhang & Chen (2022), found $L_0 = 15.3^{+46.8}_{-41.5}$ MeV. In the same vein, the authors reference larger values $L_0 = (82.32 \pm 22.93)$ MeV (Kumar et al. 2023).

Table 2. Ranges for the bulk parameters obtained from the posterior by using the different priors. All quantities are in MeV, except m_0^* (dimensionless). CI: confidence interval.

	Mean	Mode	Median	68% CI	90% CI
Uniform					
Case 1					
m_0^*	0.751	0.761	0.754	0.729 – 0.771	0.710 – 0.777
K_0	237.54	221.00	236.36	224.71 – 251.14	221.39 – 257.10
$S_{2/3}$	24.22	23.65	24.21	23.01 – 25.44	22.62 – 25.84
L_0	53.75	39.78	50.79	41.55 – 65.95	39.05 – 78.29
J	31.28	31.18	31.18	29.49 – 33.05	28.64 – 34.37
Case 2					
m_0^*	0.757	0.763	0.757	0.737 – 0.770	0.720 – 0.777
K_0	235.88	221.00	234.00	223.87 – 249.32	221.16 – 256.22
$S_{2/3}$	24.34	25.83	24.39	23.12 – 25.54	22.66 – 25.88
L_0	77.00	69.97	75.06	70.62 – 83.48	69.50 – 91.38
J	33.65	34.58	33.66	32.17 – 35.04	31.52 – 35.78
Gaussian					
Case 1					
m_0^*	0.753	0.760	0.754	0.731 – 0.770	0.714 – 0.777
K_0	237.91	237.88	237.90	227.87 – 247.94	221.25 – 254.43
$S_{2/3}$	24.25	24.28	24.26	23.37 – 25.14	22.76 – 25.73
L_0	58.01	56.32	56.73	40.96 – 72.61	33.50 – 83.82
J	31.68	31.61	31.63	29.71 – 33.56	28.60 – 34.81
Case 2					
m_0^*	0.758	0.761	0.758	0.737 – 0.770	0.722 – 0.777
K_0	236.02	236.41	236.01	225.94 – 246.12	219.49 – 252.70
$S_{2/3}$	24.34	24.36	24.34	23.44 – 25.23	22.85 – 25.81
L_0	78.03	78.07	77.94	69.67 – 86.29	64.20 – 92.65
J	33.72	33.73	33.72	32.46 – 34.99	31.62 – 35.80

Table 3. Standard values provided by Jeffrey’s scale (Jeffreys 1961), useful to compare two hypotheses by using the Bayes factor.

$\log_{10}(\mathcal{B}_{AB})$	\mathcal{B}_{AB}	Evidence against \mathcal{M}_A
< 0	> 1	Null hypothesis supported
0 to 0.5	1 to 3.2	Not worth more than a bare mention
0.5 to 1	3.2 to 10	Substantial
1 to 2	10 to 100	Strong
> 2	> 100	Decisive

4.2 Symmetric matter, pure neutron matter, and neutron star properties

At this point, we have all the probable values for the bulk parameters m_0^* , K_0 , $S_{2/3}$, L_0 , and J . In order to verify how these numbers affect nuclear and stellar matter, we use the 68% CI from the conditional probability distribution results. In addition, we also investigate the tidal deformabilities generated in the same way. The respective values of the coupling constants for these parameterizations are shown in Table A1.

In the case of symmetric nuclear matter, we analyze the obtained parametrizations in the pressure versus density plot, see Fig. 3. In these figures, the shaded areas were obtained from analysis of experimental data from nuclear collision (Danielewicz et al. 2002), and from the investigation of kaon production in heavy ion collisions (Lynch et al. 2009), respectively. We can see that the resulting EoSs satisfies the two constraint regions mentioned above. Further-

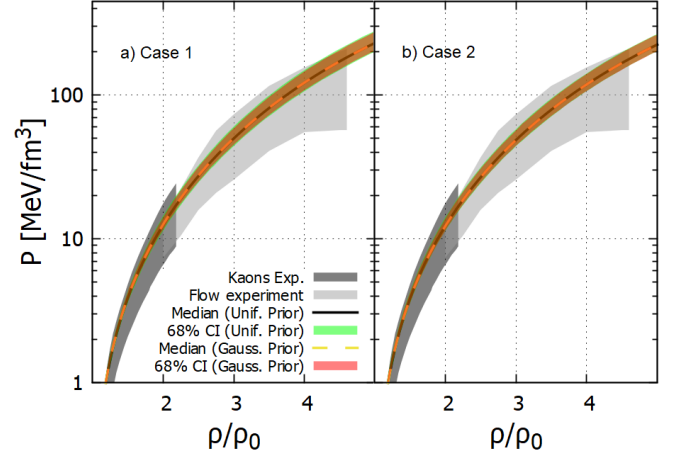


Figure 3. Pressure versus ρ/ρ_0 (symmetric matter) for the parametrizations obtained from the Bayesian analysis. The flow constraint (light gray area) was taken from (Danielewicz et al. 2002). The dark gray band was extracted from (Lynch et al. 2009). Green and red bands correspond to the parametrizations at 68% CI (posteriors) using Uniform and Gaussian priors, respectively. Full (Uniform prior used) and dashed (Gaussian prior used) curves represent those parametrizations related to the median values of the bulk parameters analyzed.

more, the description of the EoSs generated by using the results of the posterior, with the Uniform and Gaussian priors, is practically identical within 68% CI, which is evidenced by the orange region, where the description generated by each of the priors overlaps. The main difference is related to the median values, which produce an EoS closer to the edge for Case 2 when compared to Case 1.

The investigation of pure neutron matter is also important because it is a good approximation of the constituent matter in NS. In Danielewicz et al. (2002), the authors analyzed the data of the flow of particles ejected from collisions between ^{197}Au ions. The authors proposed a constraint for pressure depending on density through extrapolation of the data, including asymmetry terms with strong (*stiff*) or weak (*soft*) dependence of density on pressure. The delimited region found can be seen in Fig. 4 where, once again, it is verified that the resulting EoSs satisfy the constraint.

Still, within the scope of PNM, microscopic studies based on chiral effective field theory (chEFT) have been done over the years, see (Hebeler et al. 2013; Krüger et al. 2013; Drischler et al. 2016), for instance. In these works, low-moment expansions are used to describe the nuclear force. Interactions between nucleons are taken as point-like or via pion exchange. The corresponding parameters are adjusted through the observable of two and three bodies. In Fig. 5 it is displayed a comparison of our results, i.e., the parametrizations with 68% CI from the conditional probability distribution confronted with the bands in the energy per particle versus density plot related to chEFT calculations. We see that the parametrizations of Case 2 present greater deviations, especially for the lower-density region.

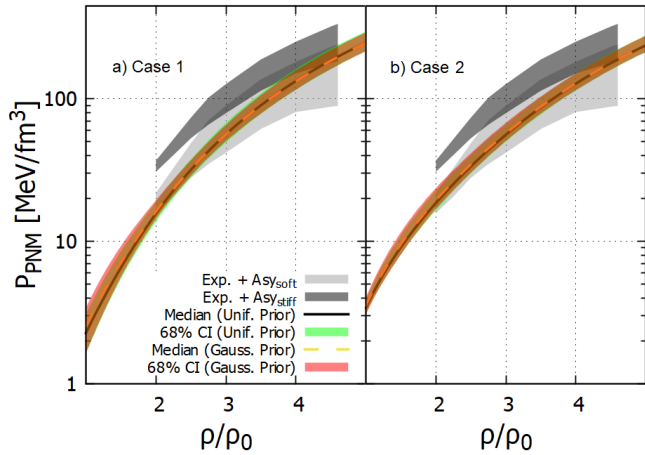
In the context of stellar matter, we investigated how the results corresponding to the EoS parameters up to 68% CI affect this system. The results for the mass-radius diagrams are shown in Fig. 6. In this figure, we also show the contours corresponding to the NICER (Miller et al. 2019; Miller et al. 2021; Riley et al. 2019, 2021) and LVC (Abbott et al. 2017, 2018) data. We can observe that Case 1 and Case 2 are very similar to each other, especially for $M/M_\odot > 1$. The inferred mass-radius relationship is also shown in Figs. 7 and 8 in relation to

Table 4. Evidence (Z) and Bayes factors, calculated through Eq. (22), for the models analysed. Model A refers to Case 1 with Uniform prior used.

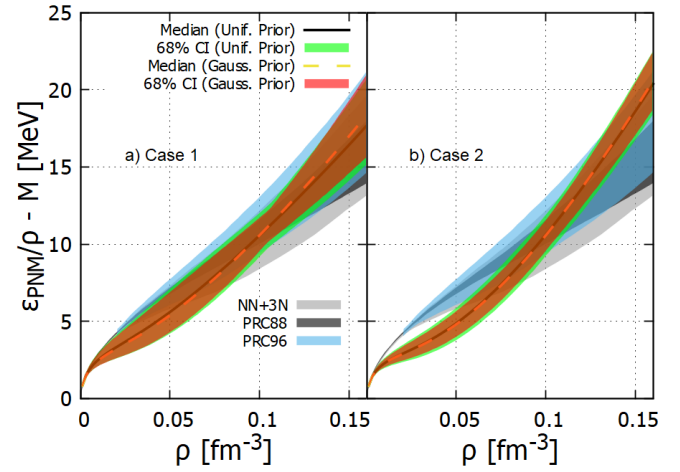
Data	Prior	Model	$\ln(Z)$	\mathcal{B}_{AB}	$\log_{10}(\mathcal{B}_{AB})$	Evidence against \mathcal{M}_A on Jeffreys' scale
Case 1	Uniform	\mathcal{M}_A	-94.06	–	–	–
Case 1	Gaussian	\mathcal{M}_B	-94.03	0.97	-0.01	Negative (supports \mathcal{M}_A)
Case 2	Uniform	\mathcal{M}_B	-95.32	3.51	0.55	Substantial
Case 2	Gaussian	\mathcal{M}_B	-95.09	2.80	0.45	Not worth more than a bare mention

Table 5. The same as in Table 4 with Model A referring to Case 1 with Gaussian prior.

Data	Prior	Model	$\ln(Z)$	\mathcal{B}_{AB}	$\log_{10}(\mathcal{B}_{AB})$	Evidence against \mathcal{M}_A on Jeffreys' scale
Case 1	Gaussian	\mathcal{M}_A	-94.03	–	–	–
Case 1	Uniform	\mathcal{M}_B	-94.06	1.03	0.01	Not worth more than a bare mention
Case 2	Uniform	\mathcal{M}_B	-95.32	3.62	0.56	Substantial
Case 2	Gaussian	\mathcal{M}_B	-95.09	2.88	0.46	Not worth more than a bare mention

**Figure 4.** Pressure versus ρ/ρ_0 (pure neutron matter) for the parametrizations obtained from the Bayesian analysis. The gray bands were taken from (Danielewicz et al. 2002). Green and red bands correspond to the parametrizations at 68% CI (posteriors) using Uniform and Gaussian priors, respectively. Full (Uniform prior used) and dashed (Gaussian prior used) curves represent those parametrizations related to the median values of the bulk parameters analyzed.

the other observables used in this article (Özel et al. 2016; Nättilä, J. et al. 2017). Note that the results also support a CI of 68% for most of the sources used in the work. However, the source described by ω Cen in Fig. 8 has a small distance from the results obtained for 68%. This distance is small for Case 1 in comparison with Case 2. This is due to the values of L_0 presented by the final ranges as results of the Bayesian analysis, as one can see in Table 2. Notice that the smaller range for L_0 is the one given by Case 1. For this case, the radii of the stars generated are also smaller in comparison with the ones obtained in Case 2, see Figs. 6 to 8. The effect of reduction of R as L_0 decreases was also verified in Fattoyev et al. (2013); Alam et al. (2016); Zhang & Li (2018); Souza et al. (2020); Lourenço et al. (2022). In Table 6 the values for the maximum properties for each prior with 68% CI are shown. The ranges of these values for the macro properties of the NS, namely, maximum mass (M_{\max}), its respective radius (R_{\max}), the radius of the $1.4M_{\odot}$ neutron star ($R_{1.4}$), and dimensionless tidal deformability of the $1.4M_{\odot}$ neutron

**Figure 5.** Energy per particle of pure neutron matter as a function of density. The grey, dark-grey, and light-blue bands, derived from chEFT, were extracted from (Hebeler et al. 2013; Krüger et al. 2013; Drischler et al. 2016). Green and red bands correspond to the parametrizations at 68% CI (posteriors) using Uniform and Gaussian priors, respectively. Full (Uniform prior used) and dashed (Gaussian prior used) curves represent those parametrizations related to the median values of the bulk parameters analyzed.

star ($\Lambda_{1.4}$) are practically the same for Uniform and Gaussian priors used in each case analyzed.

Recently, the authors of Breschi et al. (2021) have collected recent estimates for $R_{1.4}$. We display this band in Fig. 9, as well as another prediction for this quantity found in Huth et al. (2022), also from the Bayesian inference. Since all of them are estimations based on a statistical analysis taking into account 90% or more confidence intervals, we compare our results using also 90% CI. Notice that all points obtained in our work (circles) agree with these estimations, showing a trend toward values closer to the upper limits.

Finally, we calculate the dimensionless tidal deformability and depict how this quantity depends on M in Fig. 10. The description for both priors is almost identical, and we can also see that all parametrizations produce the $\Lambda_{1.4}$ inside the range predicted by LVC regardless of the case used in the Bayesian analysis. When compared to Case 1, Case 2 has slightly greater values for Λ , especially at lower values of M . For $\Lambda_{1.4}$ specifically, some studies

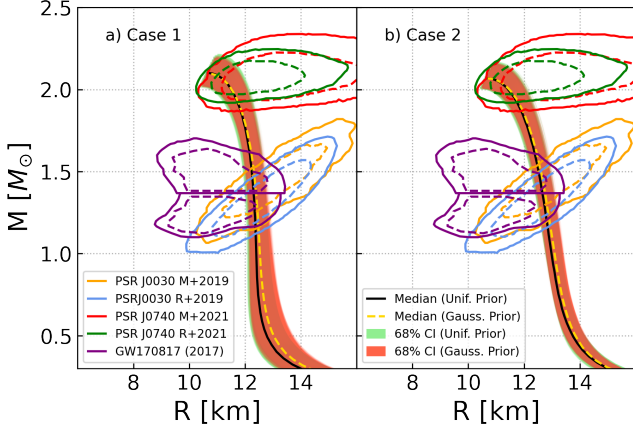


Figure 6. Mass-radius diagrams for the parametrizations obtained from the Bayesian analysis. Green and red bands correspond to the parametrizations at 68% CI (posteriors) using Uniform and Gaussian priors, respectively. Full (Uniform prior used) and dashed (Gaussian prior used) curves represent those parametrizations related to the median values of the bulk parameters analyzed. The contours for the mass-radius constrained by the NICER mission are also shown, namely, orange (Miller et al. 2019) and blue (Riley et al. 2019) ones PSR J0030+0451; red (Miller et al. 2021) and green (Riley et al. 2021) ones for PSR J0740+6620

The violet contour represents the GW170817 event (Abbott et al. 2018).

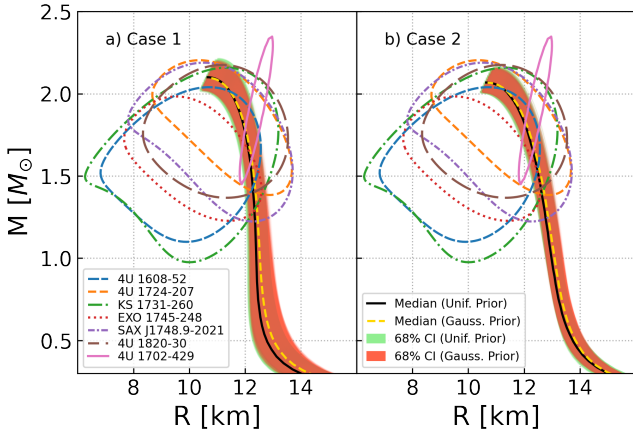


Figure 7. Same as Fig. 6, but now compared with 7 more observables used in the paper. 4U 1702-429 (Nättilä, J. et al. 2017). For the remaining ones see (Özel et al. 2016) and the references therein.

Table 6. Some macro properties resulting from the equations of state within 68% CI. See 4th column in Table 2.

	M_{\max} (M_{\odot})	R_{\max} (km)	$R_{1,4}$ (km)	$\Lambda_{1,4}$
Uniform				
Case 1	2.01 – 2.22	10.39 – 11.06	11.97 – 12.73	354.05 – 474.02
Case 2	2.00 – 2.17	10.41 – 10.98	12.34 – 13.06	378.52 – 505.15
Gaussian				
Case 1	2.00 – 2.20	10.43 – 11.02	12.04 – 12.84	357.68 – 481.32
Case 2	2.00 – 2.16	10.53 – 10.96	12.42 – 13.12	383.76 – 541.65

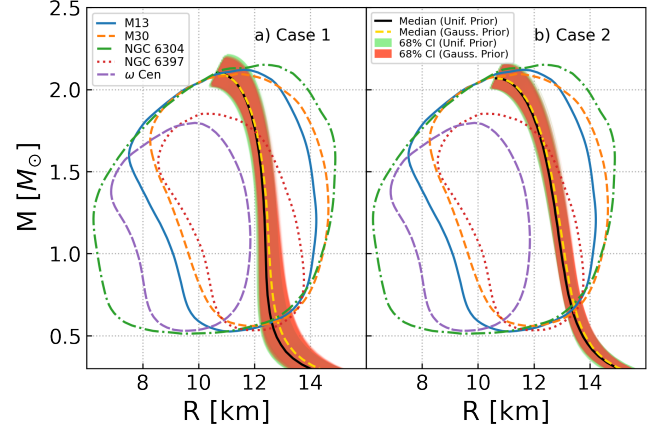


Figure 8. Same as Fig. 6, but now compared to the remaining 5 observables. See (Özel et al. 2016) and the references therein.

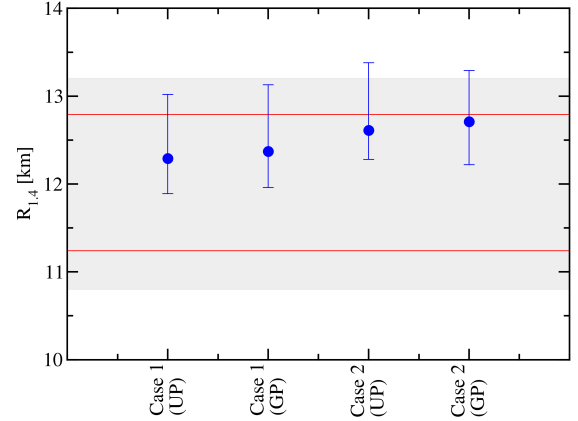


Figure 9. Predictions for $R_{1,4}$ calculated from the parametrizations obtained from the Bayesian analysis (circles). In this case, we show the results for the NS radius for $1.4M_{\text{sun}}$ at 90% CI (posteriors), when the Uniform (UP) and Gaussian (GP) priors are used

. Gray band extracted from (Breschi et al. 2021), and red lines taken from (Huth et al. 2022).

have already shown that this quantity is sensitive to L_0 (Fattoyev et al. 2013; Alam et al. 2016; Zhang & Li 2018; Souza et al. 2020; Lourenço et al. 2022). In our study, Case 2 has greater values for L_0 and as a consequence, Λ is greater in general. In Fig. 11 we show the dimensionless tidal deformability for each of the stars of the binary system related to the GW170817 event, with component masses M_1 , in the range of $1.37 \leq M_1/M_{\odot} \leq 1.60$ (Abbott et al. 2017). The mass of the companion star is calculated through the relationship between M_1 , M_2 , and the chirp mass, namely, $\mathcal{M} = (M_1 M_2)^{3/5} / (M_1 + M_2)^{1/5} = 1.188 M_{\odot}$ (Abbott et al. 2017). The deformabilities are computed using the resulting EoS within 68% CI when both priors are used. We also show contour lines at the 50% and 90% confidence intervals (purple lines) associated with the GW170817 event. We can notice that all the results obtained in this work are inside the LVC predictions.

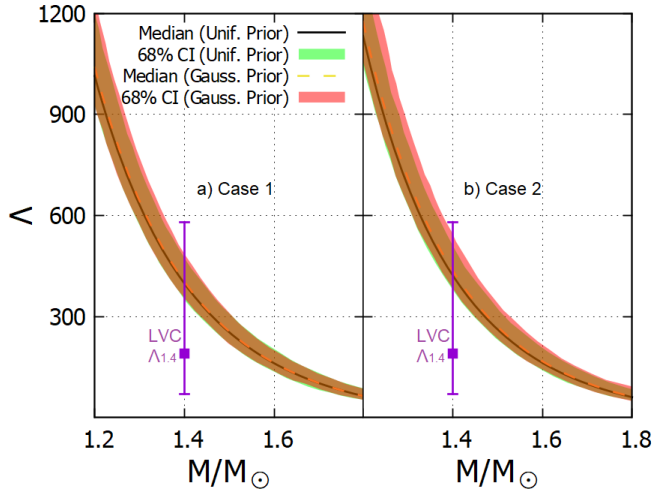


Figure 10. Λ as a function of M for the parametrizations obtained from the Bayesian analysis. Green and red bands correspond to the parametrizations at 68% CI (posteriors) using Uniform and Gaussian priors, respectively. Full (Uniform prior used) and dashed (Gaussian prior used) curves represent those parametrizations related to the median values of the bulk parameters analyzed. The purple square is the result of $\Lambda_{1,4} = 190^{+390}_{-120}$ obtained by LVC (Abbott et al. 2018).

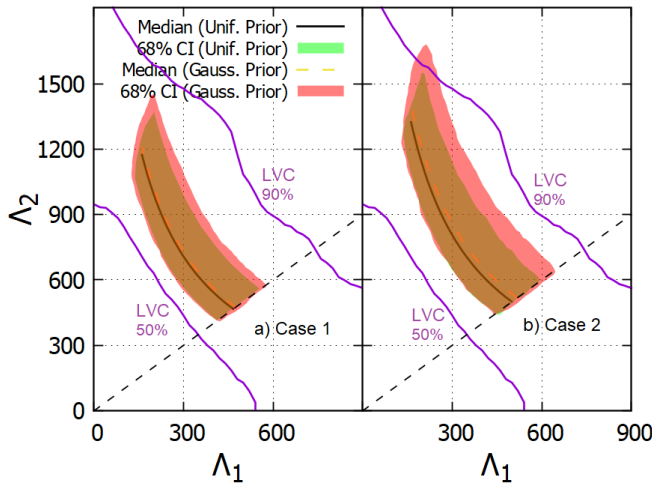


Figure 11. Dimensionless tidal deformabilities for the case of high-mass (Λ_1) and low-mass (Λ_2) components of the GW170817 event. The purple lines are the results obtained by LVC (Abbott et al. 2018) at 50% and 90% CI. The diagonal dashed lines correspond to $\Lambda_1 = \Lambda_2$. Green and red bands correspond to the parametrizations at 68% CI (posteriors) using Uniform and Gaussian priors, respectively. Full (Uniform prior used) and dashed (Gaussian prior used) curves represent those parametrizations related to the median values of the bulk parameters analyzed.

5 SUMMARY AND FINAL REMARKS

In the paper, we have performed a Bayesian analysis in order to determine ranges for the bulk parameters of nuclear matter, namely, m_0^* (effective mass ratio at $\rho = \rho_0$), K_0 (incompressibility at $\rho = \rho_0$), $S_{2/3}$ (symmetry energy at $\rho = 2\rho_0/3$), and L_0 (symmetry energy slope at $\rho = \rho_0$). For the Likelihood functions used as input for the Bayesian method, we have used 16 different sources of masses and

radii, where 11 of them were extracted from Özel et al. (2016) (6 are thermonuclear bursters called 4U 1820–30, SAX J1748.9–2021, EXO 1745–248, KS 1731–260, 4U 1724–207, and 4U 1608–52. 5 were obtained from the Quiescent Low-Mass X-ray Binaries M13, M30, NGC 6304, NGC 6397, and ω Cen), 1 taken from the neutron star X-ray analysis in 4U 1702–429 (Nättilä, J. et al. 2017), 2 components from the LVC (LSC et al. 2019), and 2 from mass-radius measurements provided by the NICER mission (Riley et al. 2019, 2021). From the ranges obtained as output, we generated the corresponding optimal parametrizations of the relativistic mean-field model used here, the one that takes into account the $\omega - \rho$ interaction in its structure. The inclusion of this term allowed us to control not only the symmetry energy but also its slope. Consequently, we were able to introduce specific values for L_0 as input in our analysis, namely, the ones inferred from the recent PREX-II experimental data (Essick et al. 2021; Estee et al. 2021; Reed et al. 2021; Yue et al. 2022).

We split our analysis into two sets named Case 1 and Case 2, both of them with two different priors, Uniform and Gaussian distributions. These sets take into account the extremes and intersections of the L_0 values obtained through the analysis of the PREX-II results aforementioned. The results show that the output values for L_0 , the ones found by the Bayesian analysis, are impacted by the choice of the distribution, more specifically, the most probable value for this quantity (mode) and its lower limit for the 68% and 90% confidence intervals for the Case 1. This occurs because the Gaussian distribution allows possible choices of lower L_0 values. The same is not true for the Uniform distribution, in which lower values for L_0 have zero probability. Our posterior results also show that for a major (minor) restriction in the input values for L_0 in the Bayesian analysis for both prior distributions, Uniform and Gaussian, Case 1 (Case 2), the output results for this quantity change considerably. For example, the posterior values using the Uniform prior are $L_0 = 50.79^{+15.16}_{-9.24}$ MeV ($L_0 = 75.06^{+8.43}_{-4.43}$ MeV) for 68% CI. These values are related to symmetry energy in the range of $J = 31.18^{+1.87}_{-1.69}$ MeV ($J = 33.66^{+1.38}_{-1.49}$ MeV), all of them compatible with values recently predicted in the literature (Adhikari et al. 2021, 2022; Reed et al. 2021; Carlson et al. 2022).

Finally, we have shown that the EoS with 68% CI obtained from the Bayesian analysis describes satisfactorily well both symmetric nuclear matter and pure neutron matter at sub- and supra-saturation density regimes. In the stellar matter, our findings show that the parameterizations produce NS with a maximum mass of $M_{\max} = (2.115 \pm 0.105)M_{\odot}$ for Case 1 and $M_{\max} = (2.085 \pm 0.085)M_{\odot}$ for Case 2, both for posterior distribution when the Uniform prior is used. The corresponding radii related to these masses are $R_{\max} = (10.725 \pm 0.335)$ km and $R_{\max} = (10.695 \pm 0.285)$ km, respectively. Furthermore, the values found for the radius of the $1.4M_{\odot}$ neutron star is $R_{1,4} = (12.35 \pm 0.38)$ km for Case 1, and $R_{1,4} = (12.7 \pm 0.36)$ km for Case 2. These values are fully compatible with those recently obtained in Breschi et al. (2021) and Huth et al. (2022). The numbers predicted by the optimal parametrizations regarding the dimensionless tidal deformabilities Λ_1 and Λ_2 (binary neutron star system), and $\Lambda_{1,4}$ (related to the $1.4M_{\odot}$ neutron star) also agrees with the observational constraints imposed by LVC from the analysis of the GW170817 event, namely, detection of gravitational waves from the merger of two neutron stars.

ACKNOWLEDGEMENTS

This work is a part of the project INCT-FNA Proc. No. 464898/2014-5, and it was financed in part by the Coordenação de Aperfeiçoamento de Pessoal de Nível Superior – Brasil (CAPES) – Finance Code 001 - (B.A.M.S., M.D.) . It is also supported by Conselho Nacional de Desenvolvimento Científico e Tecnológico (CNPq) under Grants 433369/2018-3, and 308528/2021-2 (M.D.) and 312410/2020-4 (O.L.). We also acknowledge Fundação de Amparo à Pesquisa do Estado de São Paulo (FAPESP) under Thematic Project No. 2017/05660-0 (M. D., C. H. L., and O. L.), Grant No. 2020/05238-9 (M.D., C.H.L., and O.L.) and Project 2022/03575-3 (O.L.). The authors also thank LAB-CCAM from ITA for computational support. The authors acknowledge POWER OF DATA TECNOLOGIA LTDA for providing a technological environment (big data & analytics) for data processing.

DATA AVAILABILITY STATEMENT

This manuscript has no associated data or the data will not be deposited. All data generated during this study are contained in this published article.

REFERENCES

- Abbott B. P., et al., 2017, *Phys. Rev. Lett.*, 119, 161101
 Abbott B. P., et al., 2018, *Phys. Rev. Lett.*, 121, 161101
 Abbott B., et al., 2019a, *Phys. Rev. X*, 9, 011001
 Abbott B. P., et al., 2019b, *Phys. Rev. Lett.*, 122, 061104
 Abbott B. P., et al., 2020, *Classical and Quantum Gravity*, 37, 045006
 Adhikari D., et al., 2021, *Phys. Rev. Lett.*, 126, 172502
 Adhikari D., et al., 2022, *Phys. Rev. Lett.*, 129, 042501
 Alam N., Agrawal B. K., Fortin M., Pais H., Providência C., Raduta A. R., Sulaksono A., 2016, *Phys. Rev. C*, 94, 052801
 Baym G., Pethick C., Sutherland P., 1971, *ApJ*, 170, 299
 Binnington T., Poisson E., 2009, *Phys. Rev. D*, 80, 084018
 Breschi M., Perego A., Bernuzzi S., Del Pozzo W., Nedora V., Radice D., Vescovi D., 2021, *Monthly Notices of the Royal Astronomical Society*, 505, 1661
 Cai B.-J., Li B.-A., 2016, *Phys. Rev. C*, 93, 014619
 Carlson B. V., Dutra M., Lourenço O., Margueron J., 2022, <https://arxiv.org/abs/2209.03257>
 Centelles M., Roca-Maza X., Viñas X., Warda M., 2009, *Phys. Rev. Lett.*, 102, 122502
 Chen L.-W., Ko C. M., Li B.-A., 2007, *Phys. Rev. C*, 76, 054316
 Damour T., Nagar A., 2010, *Phys. Rev. D*, 81, 084016
 Danielewicz P., Lacey R., Lynch W. G., 2002, *Science*, 298, 1592
 Drischler C., Carbone A., Hebeler K., Schwenk A., 2016, *Phys. Rev. C*, 94, 054307
 Drischler C., Furnstahl R. J., Melendez J. A., Phillips D. R., 2020, *Phys. Rev. Lett.*, 125, 202702
 Dutra M., Lourenço O., Sá Martins J. S., Delfino A., Stone J. R., Stevenson P. D., 2012, *Phys. Rev. C*, 85, 035201
 Dutra M., et al., 2014, *Phys. Rev. C*, 90, 055203
 Dutra M., Lourenço O., Menezes D. P., 2016, *Phys. Rev. C*, 93, 025806
 Essick R., Tews I., Landry P., Schwenk A., 2021, *Phys. Rev. Lett.*, 127, 192701
 Estee J., et al., 2021, *Phys. Rev. Lett.*, 126, 162701
 Fattoyev F. J., Carvajal J., Newton W. G., Li B.-A., 2013, *Phys. Rev. C*, 87, 015806
 Foreman-Mackey D., Hogg D. W., Lang D., Goodman J., 2013, *Publications of the Astronomical Society of the Pacific*, 125, 306
 Fuchs C., 2006, *Progress in Particle and Nuclear Physics*, 56, 1
 Gandolfi S., Carlson J., Reddy S., 2012, *Phys. Rev. C*, 85, 032801
 Garg U., Colò G., 2018, *Progress in Particle and Nuclear Physics*, 101, 55
 Gelman A., Carlin J., Stern H., Dunson D., Vehtari A., Rubin D., 2014, *Bayesian Data Analysis*, Third Edition. Chapman & Hall/CRC Texts in Statistical Science, Taylor & Francis
 Hebeler K., Lattimer J. M., Pethick C. J., Schwenk A., 2013, *The Astrophysical Journal*, 773, 11
 Hinderer T., 2008, *The Astrophysical Journal*, 677, 1216
 Hinderer T., Lackey B. D., Lang R. N., Read J. S., 2010, *Phys. Rev. D*, 81, 123016
 Hu B., et al., 2022, *Nature Physics*, 18, 1196
 Huth S., et al., 2022, *Nature*, 606, 276
 Jeffreys H., 1961, *The Theory of Probability*, third edn. Oxford University Press
 Kass R. E., Raftery A. E., 1995, *Journal of the American Statistical Association*, 90, 773
 Khan E., Margueron J., 2013, *Phys. Rev. C*, 88, 034319
 Krüger T., Tews I., Hebeler K., Schwenk A., 2013, *Phys. Rev. C*, 88, 025802
 Kumar M., Kumar S., Thakur V., Kumar R., Agrawal B. K., Dhiman S. K., 2023, *Phys. Rev. C*, 107, 055801
 Köhlinger F., Joachimi B., Asgari M., Viola M., Joudaki S., Tröster T., 2019, *Monthly Notices of the Royal Astronomical Society*, 484, 3126
 LSC et al., 2019, LIGO Document P1800115-v12, <https://dcc.ligo.org/LIGO-P1800115/public>
 Lattimer J. M., 2012, *Annual Review of Nuclear and Particle Science*, 62, 485
 Li B.-A., Chen L.-W., Ko C. M., 2008, *Physics Reports*, 464, 113
 Li B.-A., Cai B.-J., Xie W.-J., Zhang N.-B., 2021, *Universe*, 7
 Lourenço O., Lenzi C. H., Frederico T., Dutra M., 2022, *Phys. Rev. D*, 106, 043010
 Lynch W., Tsang M., Zhang Y., Danielewicz P., Famiano M., Li Z., Steiner A., 2009, *Progress in Particle and Nuclear Physics*, 62, 427
 Margueron J., Hoffmann Casali R., Gulminelli F., 2018, *Phys. Rev. C*, 97, 025805
 Menezes D. P., 2021, *Universe*, 7
 Miller M. C., et al., 2019, *ApJ*, 887, L24
 Miller M. C., et al., 2021, *The Astroph. J. Lett.*, 918, L28
 Näätäli, J. Miller, M. C. Steiner, A. W. Kajava, J. J. E. Suleimanov, V. F. Poutanen, J. 2017, *A&A*, 608, A31
 Oertel M., Hempel M., Klähn T., Typel S., 2017, *Rev. Mod. Phys.*, 89, 015007
 Oppenheimer J. R., Volkoff G. M., 1939, *Phys. Rev.*, 55, 374
 Özel F., Paulo F., 2016, *Annual Review of Astronomy and Astrophysics*, 54, 401
 Özel F., Psaltis D., Güver T., Baym G., Heinke C., Guillot S., 2016, *The Astroph. J.*, 820, 28
 Postnikov S., Prakash M., Lattimer J. M., 2010, *Phys. Rev. D*, 82, 024016
 Raithel C. A., Özel F., Psaltis D., 2017, *The Astrophysical Journal*, 844, 156
 Reed B. T., Fattoyev F. J., Horowitz C. J., Piekarewicz J., 2021, *Phys. Rev. Lett.*, 126, 172503
 Reinhard P.-G., Roca-Maza X., Nazarewicz W., 2021, *Phys. Rev. Lett.*, 127, 232501
 Riley T. E., et al., 2019, *Astrophys. J. Lett.*, 887, L21
 Riley T. E., et al., 2021, *The Astrophysical Journal Letters*, 918, L27
 Robert C. P., Chopin N., Rousseau J., 2009, *Statistical Science*, 24, 141
 Salinas M., Piekarewicz J., 2023, Bayesian refinement of covariant energy density functionals, <https://arxiv.org/abs/2301.09692>
 Santos B. M., Dutra M., Lourenço O., Delfino A., 2015, *Phys. Rev. C*, 92, 015210
 Sivia D., Skilling J., 2006, *Data Analysis: A Bayesian Tutorial*. Oxford science publications, OUP Oxford
 Souza L. A., Dutra M., Lenzi C. H., Lourenço O., 2020, *Phys. Rev. C*, 101, 065202
 Steiner A. W., Lattimer J. M., Brown E. F., 2010, *The Astrophysical Journal*, 722, 33
 Steiner A. W., Lattimer J. M., Brown E. F., 2016, *European Physical Journal A*, 52, 18
 Tolman R. C., 1939, *Phys. Rev.*, 55, 364
 Traversi S., Char P., Pagliara G., 2020, *The Astroph. J.*, 897, 165
 Typel S., 2018, *Particles*, 1, 3
 Vidaña I., Providência C., Polls A., Rios A., 2009, *Phys. Rev. C*, 80, 045806

Table A1. Coupling constants related to the parametrizations in which the bulk parameters are shown in Table 2.

	$g_{\sigma}^2/m_{\sigma}^2$ (fm ²)	$g_{\omega}^2/m_{\omega}^2$ (fm ²)	g_{ρ}^2/m_{ρ}^2 (fm ²)	$100A/g_{\sigma}^3$ (fm ⁻¹)	B/g_{σ}^4 (10 ⁻³)	10α
Uniform						
Case 1						
Mean	10.94	5.81	6.85	-3.13	-4.56	1.00
Mode	10.84	5.51	7.47	-3.86	-6.85	1.73
Median	10.88	5.74	7.00	-3.23	-4.65	1.12
68% L.L.	11.76	6.48	7.12	-2.83	-5.93	1.41
68% U.L.	10.18	5.24	6.99	-3.23	-0.80	0.75
90% L.L.	12.34	7.03	7.39	-2.47	-5.69	1.49
90% U.L.	9.90	5.04	6.84	-3.15	1.68	0.49
Case 2						
Mean	10.79	5.65	6.09	-3.32	-4.62	0.42
Mode	10.8	5.48	7.07	-3.90	-6.85	0.62
Median	10.80	5.63	6.16	-3.38	-4.89	0.46
68% L.L.	11.54	6.25	5.61	-3.03	-6.17	0.48
68% U.L.	10.22	5.25	6.55	-3.28	-1.22	0.36
90% L.L.	12.06	6.74	5.39	-2.68	-5.99	0.47
90% U.L.	9.92	5.06	6.56	-3.18	1.37	0.23
Gaussian						
Case 1						
Mean	10.90	5.77	6.67	-3.16	-4.47	0.88
Mode	10.67	5.54	6.76	-3.36	-4.17	0.97
Median	10.85	5.72	6.73	-3.20	-4.42	0.92
68% L.L.	11.66	6.41	7.37	-2.83	-5.68	1.42
68% U.L.	10.23	5.24	6.63	-3.33	-1.46	0.58
90% L.L.	12.23	6.92	8.46	-2.55	-5.81	1.84
90% U.L.	9.93	5.05	6.65	-3.25	1.04	0.37
Case 2						
Mean	10.76	5.62	6.06	-3.35	-4.57	0.40
Mode	10.67	5.53	6.08	-3.42	-4.38	0.40
Median	10.77	5.62	6.06	-3.34	-4.58	0.40
68% L.L.	11.49	6.22	5.80	-3.02	-5.98	0.51
68% U.L.	10.25	5.24	6.33	-3.39	-1.83	0.29
90% L.L.	12.03	6.69	5.67	-2.74	-6.17	0.60
90% U.L.	9.94	5.04	6.50	-3.32	0.71	0.21

Yue T.-G., Chen L.-W., Zhang Z., Zhou Y., 2022, *Phys. Rev. Res.*, 4, L022054

Yukawa H., 1935, Proceedings of the Physico-Mathematical Society of Japan. 3rd Series, 17, 48

Zhang Z., Chen L.-W., 2022, Bayesian Inference of the Symmetry Energy and the Neutron Skin in ⁴⁸Ca and ²⁰⁸Pb from CREX and PREX-2 ([arXiv:2207.03328](https://arxiv.org/abs/2207.03328))

Zhang N.-B., Li B.-A., 2018, *Journal of Physics G: Nuclear and Particle Physics*, 46, 014002

Zhu Z., Li A., Liu T., 2022, A Bayesian inference of relativistic mean-field model for neutron star matter from observation of NICER and GW170817/AT2017gfo, <https://arxiv.org/abs/2211.02007>

APPENDIX A: EOS COUPLING CONSTANTS

In Table A1 we furnish the coupling constants for the parametrizations that produce the nuclear bulk parameters presented in Table 2.

This paper has been typeset from a $\text{\TeX}/\text{\LaTeX}$ file prepared by the author.